

# Genetically encoded biosensors for visualizing live-cell biochemical activity at super-resolution

Gary C H Mo<sup>1</sup>, Brian Ross<sup>1,2</sup>, Fabian Hertel<sup>1</sup>, Premashis Manna<sup>3,4</sup>, Xinxing Yang<sup>5</sup>, Eric Greenwald<sup>1</sup>, Chris Booth<sup>1</sup>, Ashlee M Plummer<sup>6</sup>, Brian Tenner<sup>5</sup>, Zan Chen<sup>7</sup>, Yuxiao Wang<sup>8</sup>, Eileen J Kennedy<sup>8</sup>, Philip A Cole<sup>7</sup>, Karen G Fleming<sup>6</sup>, Amy Palmer<sup>4,9</sup>, Ralph Jimenez<sup>3,4</sup>, Jie Xiao<sup>5</sup>, Peter Dedecker<sup>10</sup> & Jin Zhang<sup>1,7</sup>

**Compartmentalized biochemical activities are essential to all cellular processes, but there is no generalizable method to visualize dynamic protein activities in living cells at a resolution commensurate with cellular compartmentalization. Here, we introduce a new class of fluorescent biosensors that detect biochemical activities in living cells at a resolution up to threefold better than the diffraction limit. These 'FLINC' biosensors use binding-induced changes in protein fluorescence dynamics to translate kinase activities or protein–protein interactions into changes in fluorescence fluctuations, which are quantifiable through stochastic optical fluctuation imaging. A protein kinase A (PKA) biosensor allowed us to resolve minute PKA activity microdomains on the plasma membranes of living cells and to uncover the role of clustered anchoring proteins in organizing these activity microdomains. Together, these findings suggest that biochemical activities of the cell are spatially organized into an activity architecture whose structural and functional characteristics can be revealed by these new biosensors.**

Coordinated protein assembly and biochemical activity at specific loci in living cells are responsible for functional changes in cell growth, division, migration or programmed death. The emerging picture indicates that these biochemical activities are dynamically regulated in various temporal waveforms<sup>1,2</sup> and are spatially organized into distinct micro- or nanodomains<sup>3–5</sup>. This concept suggests that, in addition to maintaining their physical structure, cells also maintain an 'activity architecture' composed of organized activated molecules and their regulatory partners. This model has not been directly tested, and critical questions about the spatial organization of biochemical activities remain. The classical example of compartmentalized signaling is that of PKA, wherein A kinase–anchoring proteins (AKAPs) anchor<sup>3</sup> the

PKA holoenzyme into signaling microdomains. However, this compartmentalization is achieved through the regulatory (R) subunits of PKA rather than through its catalytic (C) subunits. PKA stimulation and subsequent release and diffusion of the C subunit would diminish this spatial compartmentalization. Therefore, even in this classical model, it is unclear whether and how the kinase's activity is spatially organized in living cells. Many super-resolution imaging methods have emerged that are able to reveal the location of nanoscale cellular features<sup>6,7</sup> with vastly improved spatial resolution; such methods include stimulated emission depletion (STED)<sup>8</sup>, photoactivated localization microscopy or stochastic optical reconstruction microscopy (PALM/STORM)<sup>9,10</sup>, stochastic optical fluctuation imaging (SOFI) and photochromic SOFI (pcSOFI)<sup>11,12</sup>, and structured illumination microscopy (SIM)<sup>13</sup>. Although there have been considerable efforts to develop applications of super-resolution imaging beyond biomolecule localization<sup>14–16</sup>, there is no general methodology to visualize dynamic biochemical activities such as protein–protein interactions (PPI) and post-translational modifications in live cells at super-resolution. Here, we addressed this need by introducing a new class of generalizable genetically encodable biosensors, which enable what is, to our knowledge, the first direct super-resolution visualization of dynamic biochemical activities. Through use of these new biosensors in combination with STORM, we obtained direct evidence of highly active PKA activity microdomains in the plasma membrane.

## RESULTS

### Discovery and characterization of FLINC

Classic fluorescence resonance energy transfer (FRET)-based reporters are characterized by proximity-dependent changes in the fluorescence signals of both donor and acceptor fluorophores<sup>17</sup>. In contrast, the reporters used in our super-resolution activity-imaging function through a phenomenon that we term

<sup>1</sup>Department of Pharmacology, University of California San Diego, La Jolla, California, USA. <sup>2</sup>Department of Biomedical Engineering, Johns Hopkins University, Baltimore, Maryland, USA. <sup>3</sup>JILA, University of Colorado and NIST, Boulder, Colorado, USA. <sup>4</sup>Department of Chemistry and Biochemistry, University of Colorado, Boulder, Colorado, USA. <sup>5</sup>Department of Biophysics and Biophysical Chemistry, The Johns Hopkins University School of Medicine, Baltimore, Maryland, USA. <sup>6</sup>T. C. Jenkins Department of Biophysics, Johns Hopkins University, Baltimore, Maryland, USA. <sup>7</sup>Department of Pharmacology and Molecular Sciences, The Johns Hopkins University School of Medicine, Baltimore, Maryland, USA. <sup>8</sup>Department of Pharmaceutical and Biomedical Sciences, University of Georgia, Athens, Georgia, USA. <sup>9</sup>BioFrontiers Institute, University of Colorado, Boulder, Colorado, USA. <sup>10</sup>Department of Chemistry, KU Leuven, Heverlee, Belgium. Correspondence should be addressed to J.Z. (jzhang32@ucsd.edu).

fluorescence fluctuation increase by contact (FLINC). In FLINC, the proximity of two fluorescent proteins changes the fluorescence fluctuation behavior of the readout protein, thereby enabling super-resolution imaging with pcSOFI.

This FLINC phenomenon was initially discovered by examination of the fluorescence dynamics of TagRFP-T in a series of plasma-membrane-tethered constructs. We observed that the proximity of Dronpa<sup>18</sup> significantly increases the fluorescence fluctuations of TagRFP-T<sup>19</sup> (Supplementary Video 1). We characterized this phenomenon by using Dronpa–TagRFP-T (DpTT), in which these two fluorescent proteins (FPs) are directly fused together by a short flexible linker. Several characteristics were revealed. First, fluctuations were easily detected in live cells expressing membrane-targeted DpTT (Fig. 1a and Supplementary Fig. 1). The single-molecule fluorescence fluctuations generated by purified DpTT were quantitatively more robust than those from TagRFP-T (Fig. 1b). Second, this effect occurred specifically between tethered Dronpa and TagRFP-T (Fig. 1c). Third, the external residues of Dronpa, not its chromophore, were key determinants of this effect (Fig. 1d, Supplementary Fig. 1 and Supplementary Note). Finally, decreasing the distance between Dronpa and TagRFP-T by using rigid helical linkers of successively shorter lengths<sup>20</sup> results in a corresponding increase in TagRFP-T fluorescence fluctuations (Fig. 1e), thus indicating an effective range of 5–6 nm.

Despite a low intrinsic affinity between Dronpa and TagRFP-T (Supplementary Fig. 2,  $K_d = 159\text{--}917\ \mu\text{M}$ ), the high effective concentrations in the fusions facilitated their intramolecular binding. Whereas TagRFP-T, like many FPs, ‘blinks’ stochastically<sup>21,22</sup>, the specific binding of Dronpa alters the blinking behavior of TagRFP-T, thus making a larger percentage (25%) of TagRFP-T undergo dark-state conversion at a 25% faster rate (Supplementary Fig. 3). This photophysical mechanism gives rise to the modulated single-molecule fluorescence fluctuation that can be used to assess whether Dronpa is in proximity to TagRFP-T (Supplementary Note).

### FLINC-based biosensors

FLINC formed the basis of our new class of fluorescent biosensors that can be used to generate super-resolution activity maps via pcSOFI. In pcSOFI, time series of fluorescence images are recorded to obtain many single-molecule fluctuations across the field of view. Pairwise cross-cumulants, calculated with the appropriate pixel pairings, yield an autocorrelation-like ‘pcSOFI value’ at subpixel resolution that can be used to quantify the strength of fluctuation<sup>23</sup> with a high signal-to-noise ratio (Supplementary Fig. 4). The collection of pcSOFI values constitute a quantitative image that provides a super-resolution map of the biochemical activity under study.

We modeled FLINC-based activity biosensors after FRET-based biosensors, which serve as surrogate substrates of the kinase of interest. Phosphorylation of these biosensors leads to a change in fluorescence properties, thereby allowing kinase activity to be monitored by imaging a reporter, without labeling or disrupting the active kinase. In the FLINC-based PKA biosensor, we combined the molecular switch in an A kinase–activity reporter (AKAR)<sup>24</sup> with an EV linker (AKARev)<sup>25</sup> with Dronpa and TagRFP-T into FLINC–AKAR1 (targeted to the plasma membrane). Here, FLINC was affected in a phosphorylation-dependent manner, such that high pcSOFI values indicated high PKA

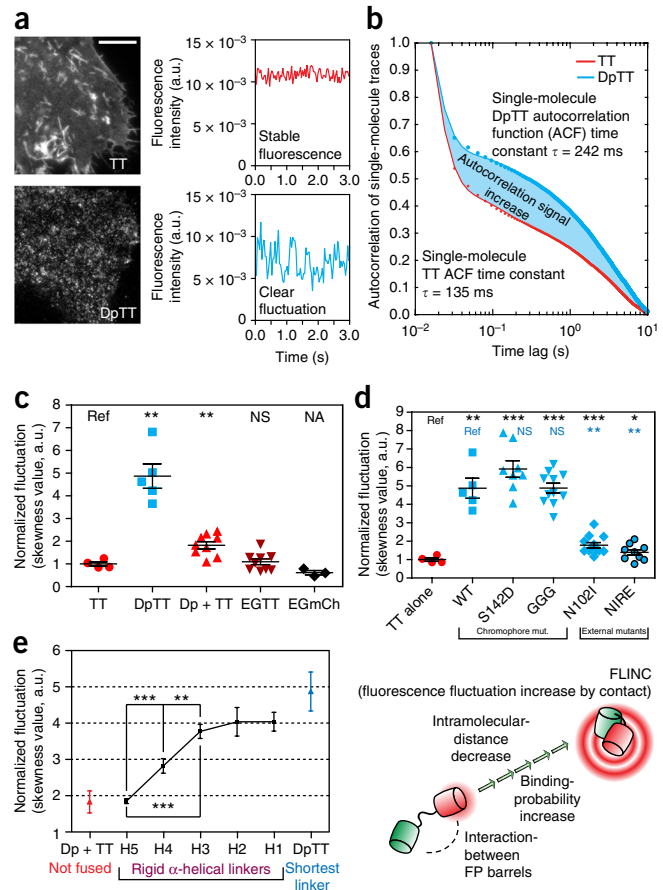


**Figure 1** | TagRFP-T (TT) red fluorescence fluctuations increase with Dronpa (Dp) proximity in a distance-dependent manner. **(a)** Representative images and single-pixel fluorescence intensity traces in HeLa cells expressing DpTT (Dronpa–linker–TagRFP-T),  $n = 7$  cells) and TagRFP-T alone ( $n = 8$ ), excited by a 561-nm laser. A.u., arbitrary units. Scale bar, 10  $\mu\text{m}$ . **(b)** Aggregated mean normalized autocorrelation function (ACF) of many single-molecule fluorescence traces from purified fluorescent DpTT and TagRFP-T. The amplitude increase demonstrates the clear gain in autocorrelation signal from increased millisecond fluctuations of DpTT. **(c)** Quantified fluctuation in various constructs, demonstrating the specific nature of the fluctuation increase. TT ( $n = 8$ ), DpTT ( $n = 7$ ), Dp + TT ( $n = 9$ ), EGTT (EGFP–linker–TagRFP-T,  $n = 8$ ) and EGFP–linker–mCherry (EGmCh,  $n = 9$ ) were analyzed. **(d)** Quantified fluctuation in various mutant constructs, demonstrating that Dronpa’s chromophore is not involved, but external Dronpa residues are important for the phenomenon. TT alone ( $n = 8$ ), WT ( $n = 7$ ); chromophore mutants (mut) Dp<sup>S142D</sup>–TT (S142D,  $n = 8$ ) and Dp<sup>C62G Y63G</sup>–TT (GGG,  $n = 11$ ); and FP surface mutants Dp<sup>N102I</sup>–TT (N102I,  $n = 12$ ) and Dp<sup>N102I R149E</sup>–TT (NIRE,  $n = 9$ ) were analyzed. **(e)** A variable number of rigid helical repeats permit measurement of distance dependence and sensitivity of changes in fluctuation.  $H_n$ , number of rigid (EAAAK) repeats; DpTT (short linker) and Dp + TT (not fused) were included as comparisons. H2–H5 linkers are shown with the nominal FP distances reported in the literature. All constructs in **e** were targeted to the plasma membranes of HeLa cells by the lyn sequence and examined for the following: DpTT ( $n = 5$ ), H1 ( $n = 7$ ), H2 ( $n = 6$ ), H3 ( $n = 14$ ), H4 ( $n = 17$ ), H5 ( $n = 10$ ) and Dp + TT ( $n = 9$ ). Pairwise  $t$ -test results in **c–e** are shown for data compared with the reference (ref) construct. NA, not applicable; NS, not significant;  $*P < 0.05$ ;  $**P < 0.01$ ;  $***P < 0.001$ . In all dot plots and **e**, center line and whiskers mark the average and s.e.m., respectively.

activities (Fig. 2a). By normalizing the pcSOFI values to correct for uneven biosensor distribution (Supplementary Note and Supplementary Fig. 5a–e), we were able to quantify PKA activity

both at the single-pixel level and averaged across the entire cell. The average normalized pcSOFI value rapidly increased in the first minute after PKA activation in HeLa cells treated with a cocktail of the adenylyl cyclase activator forskolin (Fsk) and phosphodiesterase inhibitor 3-isobutyl-1-methylxanthine (IBMX), reaching a plateau at a 25–39% increase after 7–10 min (Fig. 2b–d) and showing a dynamic range of up to a 40% increase. Addition of the PKA-specific inhibitor H-89 (20  $\mu$ M) gradually decreased the average normalized pcSOFI value, thus demonstrating the reversibility. Additional experiments using a negative control biosensor that could not be phosphorylated (Fig. 2c,d) and the membrane-targeted PKA inhibitor PKI (Fig. 2c) demonstrated that the response was dependent on phosphorylation of the biosensor and PKA activity, respectively. Time courses with H-89 inhibition and a submaximal dose of Fsk (Supplementary Fig. 6) showed that FLINC–AKAR1 accurately reported over a range of PKA activity. We initially quantified PKA activity every 5 min (Fig. 2c) and, after further development, every 30 s (Fig. 2d). The kinetics of PKA stimulation, as monitored by FRET-based or FLINC-based AKAR, showed no significant differences (FRET half-time ( $t_{1/2}$ ) = 1.2 min, number of cells ( $n$ ) = 7; FLINC  $t_{1/2}$  = 0.73 min,  $n$  = 4). Importantly, our analysis of FLINC–AKAR1 fluctuations generated super-resolution images of PKA activity at each time point throughout the treatment course. Monitoring the same profile line in the normalized pcSOFI images before and after Fsk/IBMX treatment (Fig. 2e) indicated that subdiffraction-limit activity features (Fig. 2f) that responded to stimulation were resolved. Actin-targeted FLINC–AKAR1 enabled us to distinguish the stimulated PKA activity with an average Gaussian full width at half maximum of  $179 \pm 6$  nm ( $n$  = 7) and  $116 \pm 6$  nm ( $n$  = 7) (mean  $\pm$  s.e.m.), in agreement with the respective use of second- and third-order analyses (Supplementary Fig. 7a,b). Furthermore, we were able to resolve the stimulated membrane PKA activity in converging filopodial features separated by 160 nm and 107 nm, by using second- and third-order cumulant analyses, respectively (Supplementary Note and Supplementary Fig. 7c,d). Under the conditions used here (Supplementary Note), biosensor diffusion did not affect the temporal and spatial resolution of pcSOFI<sup>11</sup>, and its accurate quantification of FLINC. Thus, as a reporter of kinase activity, FLINC–AKAR1 not only provides a consistent readout for PKA activity but also allows for monitoring of the dynamic changes of PKA activity with high contrast at super-resolution.

### PKA activity microdomains

The PKA activity maps generated by FLINC–AKAR1 revealed many minute and highly active punctate features on the basal membranes of living cells. These activity puncta, with a mean diameter of 350 nm (Supplementary Note), were clearly resolved after Fsk/IBMX stimulation. Activation of PKA induced a twofold increase in microdomain coverage over the basal membrane, but this induction was not observed with the DpTT control or the nonphosphorylatable mutant (TA) (Fig. 2g). Using direct stochastic optical reconstruction microscopy (dSTORM) in total internal reflection fluorescence (TIRF) conditions, we further verified the presence of these highly active PKA microdomains (Supplementary Note). Phospho-PKA substrates (p-PKAsubs) were clearly clustered (Supplementary Fig. 8a,b), forming distinct microdomains with a mean diameter of approximately 250 nm on the basal membrane (Supplementary Fig. 8c and Supplementary Note).

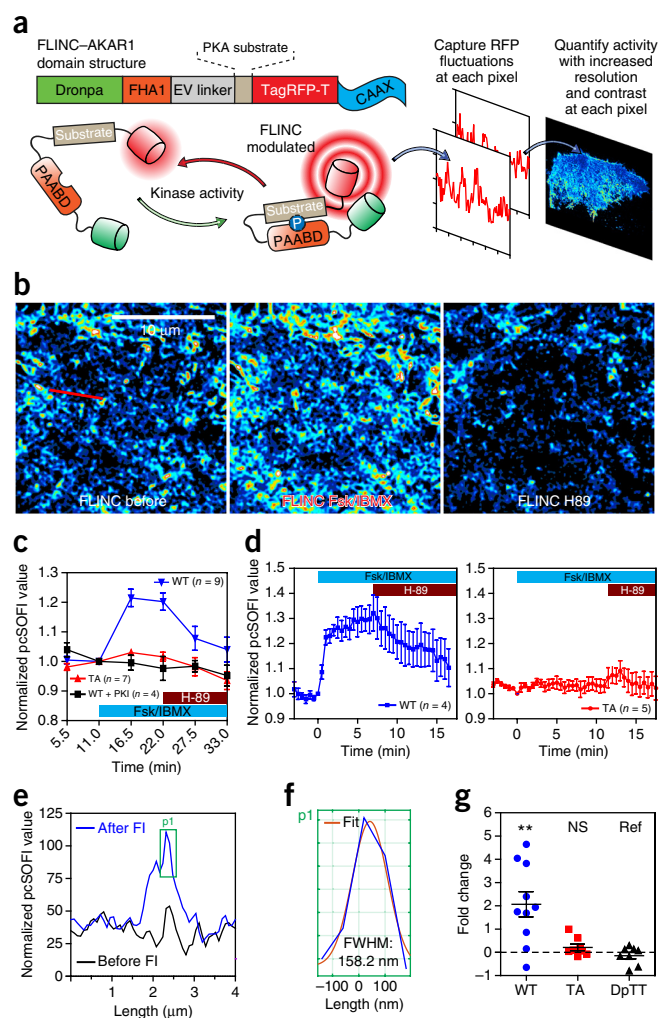


**Figure 2** | FLINC resolves PKA activity microdomains on the plasma membrane at super-resolution. (a) Schematic of the FLINC–AKAR1 design principle, the domain structure of FLINC–AKAR1 and the acquisition of super-resolution activity images with pcSOFI. (b) FLINC–AKAR1 super-resolution images clearly resolve the response to Fsk/IBMX stimulation (Fsk 50  $\mu$ M and IBMX 100  $\mu$ M) and inhibition (H-89 20  $\mu$ M), and detailed spatial information on membrane PKA activity emerges. Color scales are identical. (c) Mean normalized pcSOFI response time course from live HeLa cells expressing WT ( $n$  = 9 cells) FLINC–AKAR1, nonphosphorylatable mutant (TA,  $n$  = 7) and WT coexpressed with PKI (WT + PKI,  $n$  = 4), after PKA stimulation and inhibition. (d) The normalized pcSOFI response time course from live HeLa cells expressing WT ( $n$  = 4) FLINC–AKAR1 and nonphosphorylatable mutant (TA,  $n$  = 5), after PKA stimulation and inhibition, determined with a fast acquisition imaging scheme. (e) A profile line at the same position across the pcSOFI images before and after Fsk/IBMX (FI) stimulation clearly demonstrates sensing of PKA activity at super-resolution; the profile is marked by a red line in b. (f) Zoom view of the active PKA feature (p1) in f, showing resolution of the Gaussian fitting and full width at half maximum (FWHM) size of this subdiffraction-limit PKA activity microdomain. (g) Comparison of the changes in the fraction of membrane area occupied by punctate structures after stimulation across various FLINC constructs, all targeted with the same CAAX motif. In FLINC–AKAR1 experiments, cells (WT,  $n$  = 10; TA,  $n$  = 8) were stimulated with Fsk/IBMX; in DpTT experiments, cells ( $n$  = 8) received no drug treatment. Unless indicated otherwise, pairwise  $t$ -test results are shown for data compared with the reference (ref) construct. NS, not significant; \*\* $P$  < 0.01. In c and d, center line and whiskers mark the average and s.e.m., respectively.

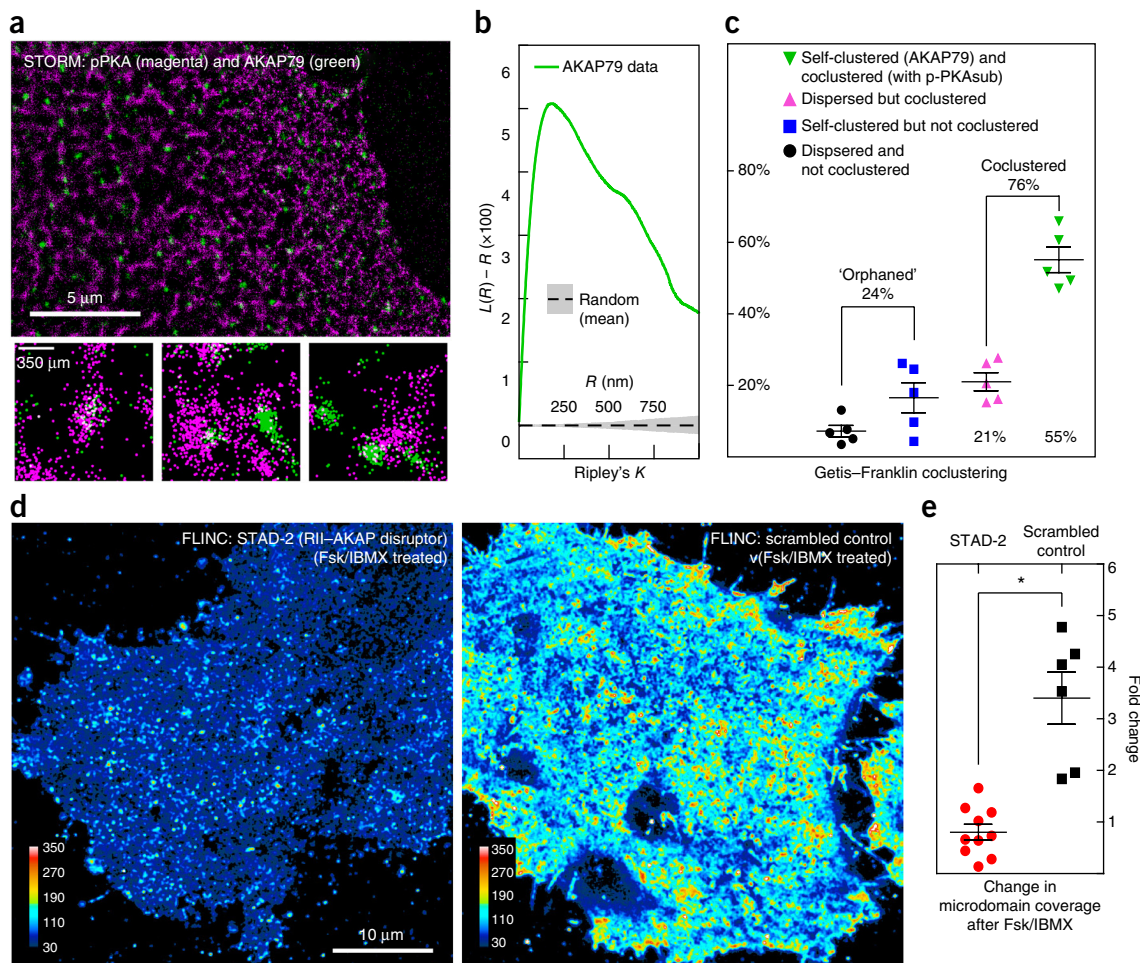


**Figure 3** | A kinase-anchoring proteins (AKAPs) are coclustered with PKA activity microdomains and are required for microdomain formation. (a) A representative two-color STORM image of p-PKAsub (magenta) and AKAP79 (green), with specific examples of the p-PKAsub/AKAP79 relationship shown beneath. (b) ( $n = 5$  cells) Ripley's  $K$  analysis of AKAP79 localizations shows clear clustering above random sampling. (c) Getis-Franklin coclustering analyses of the two-color STORM images, identifying populations with different p-PKAsub/AKAP79 relationships; the majority ( $55 + 21 = 76\%$ ) of AKAP79 is associated with p-PKAsub ( $n = 5$ ). (d) Representative live-cell super-resolution FLINC-AR1 images of stimulated PKA activity after the disruption of AKAP-PKA RII interactions with a synthetic AKAP disruptor, STAD-2 ( $n = 10$ ), in comparison with its scrambled control ( $n = 6$ ). Scale bar, 10  $\mu\text{m}$ . The color scales are identical. (e) The effect of RII-AKAP disruption on PKA activity microdomains, quantified by fold change in microdomain coverage. Cells were pretreated with either STAD-2 ( $n = 10$ ) or scrambled peptide control ( $n = 6$ ) before Fsk/IBMX stimulation. Unless indicated otherwise, pairwise  $t$ -test results are shown for data compared with the reference (ref) construct.  $*P < 0.05$ . In c and e, center line and whiskers mark the average and s.e.m., respectively.

The basal membranes of cells stimulated by Fsk/IBMX again displayed a significant 4.8-fold increase in p-PKAsub clusters per unit membrane area (Supplementary Fig. 8d). All these characteristics observed in STORM were consistent with those observed with FLINC-AR1 in live cells. Thus, despite the conventionally held views of rapid cAMP diffusion<sup>26–30</sup> and mobility of PKA catalytic subunits<sup>31,32</sup>, PKA activity was not uniform but instead was confined within microdomains on the plasma membranes of living mammalian cells.

#### Clustered anchoring proteins spatially organize PKA activity microdomains

AKAPs are critical components of PKA compartmentalization. We set out to directly determine the precise spatial relationship between highly active PKA microdomains and the loci of specific PKA anchoring. AKAP79/AKAP5 is a doubly lipidated, predominantly membrane-localized scaffold that associates with RII

PKA holoenzymes and other regulators of PKA signaling<sup>33,34</sup>. Two-color STORM imaging in fixed cells (Supplementary Fig. 9a,b) showed that AKAP79 was itself highly clustered (Fig. 3a,b and Supplementary Fig. 9c), with a mean diameter of 127 nm. Getis-Franklin coclustering (Supplementary Note and Supplementary Fig. 9d) demonstrated a high degree of spatial correlation between AKAP79 and p-PKAsub (Fig. 3c). 76% of total AKAP79 localizations, whether in clusters or dispersed, were associated with p-PKAsub microdomains. Surprisingly, however, a total of 24% of AKAP79 localizations were not associated with p-PKAsubs, thus suggesting that AKAP-mediated complexes are heterogeneous and that a subpool of these complexes may be differentially regulated, for example, because of differences in phosphatase activity. Through a combination of AKAP79 localization and FLINC-AR1 imaging in the same cells, we observed characteristics that are similar to those reported above. Substantial overlap with PKA activity microdomains was observed above

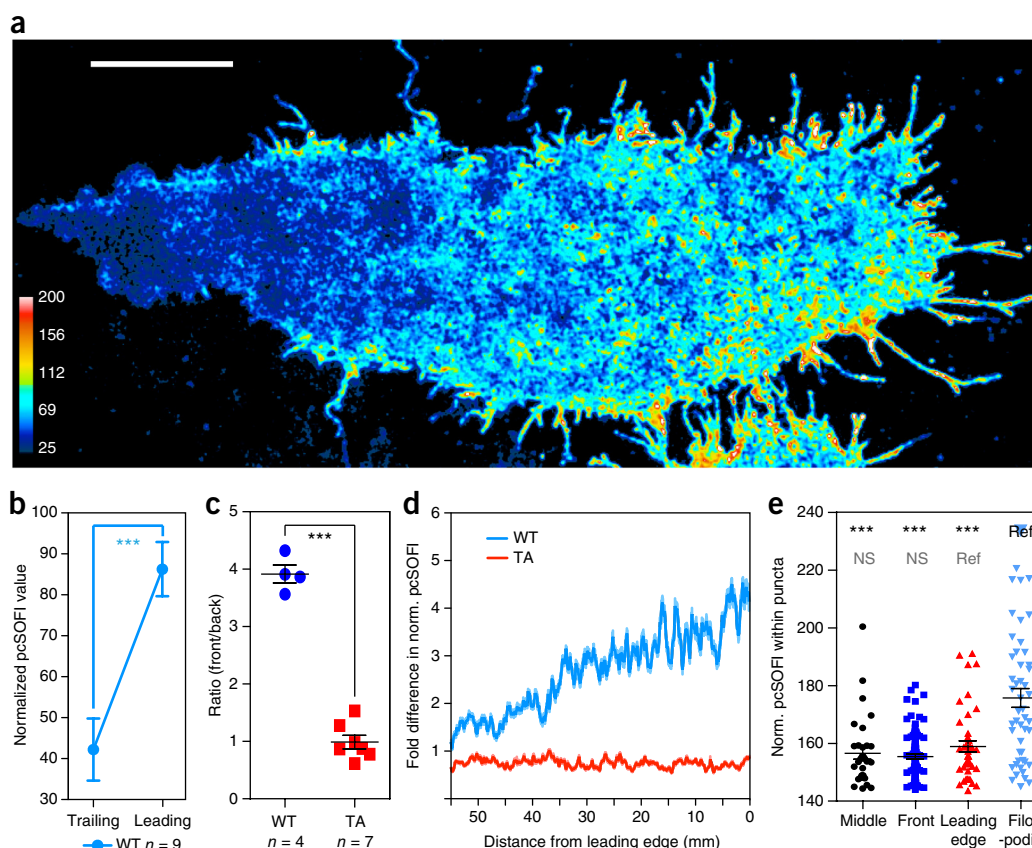


**Figure 4** | PKA activity gradient of a migrating cell at super-resolution. **(a)** The PKA activity gradient in a migrating  $\alpha 4$ CHO cell expressing WT FLINC-AKAR1. Scale bar, 10  $\mu$ m. **(b)** Average normalized (norm) pcSOFI values within leading- and trailing-edge regions of migrating cells show clearly different PKA activities. **(c)** Migrating  $\alpha 4$ CHO cells expressing WT FLINC-AKAR1, compared with cells expressing a nonphosphorylatable TA mutant, show a significant gradient in terms of normalized pcSOFI values. Pairwise *t*-test results are shown. **(d)** Representative PKA activity profile ( $n = 9$  cells) observed along the migration direction, for FLINC-AKAR1 and its TA mutant. **(e)** Representative data ( $n = 9$ ) showing that active microdomains within the filopodia have significantly higher PKA activity than that elsewhere on the basal membrane of migrating CHO cells; basal-membrane regions are indicated according to their increasing distance from the leading edge of the migration direction (filopodia, leading edge, front and middle) ( $n = 9$ ). Unless indicated otherwise, pairwise *t*-test results are shown for data compared with the reference (ref) construct. NS, not significant; \*\*\* $P < 0.001$ . In **c** and **e**, center line and whiskers mark the average and s.e.m., respectively.

random clustering (**Supplementary Fig. 9c**), and we again observed so-called ‘orphaned’ AKAP79 molecules.

Next we tested whether, beyond a high degree of spatial correlation, AKAP anchoring is required for the formation of highly active membrane PKA microdomains in living HeLa cells. To this end, we used the synthetic peptide STAD-2, which specifically disrupts the interaction between AKAPs and the PKA regulatory subunit RII isoform<sup>35</sup>. In agreement with previous observations, the membrane PKA activity in living cells pretreated with STAD-2 was low after Fsk/IBMX stimulation (**Supplementary Fig. 10**) and was devoid of highly active PKA microdomains, in contrast with cells treated with scrambled peptide (**Fig. 3d,e**). These live-cell data indicated that, beyond a high degree of spatial correlation, PKA activity microdomains require anchoring by AKAPs such as AKAP79.

#### Polarized distribution of activity microdomains

Having confirmed that cells do maintain a well-structured PKA spatial signaling architecture, we next examined the presence and organization of highly active PKA microdomains during integrin-dependent cell migration, which requires effective

polarization. Chinese hamster ovary cells stably expressing  $\alpha 4$  integrin ( $\alpha 4$ CHO) exhibit a gradient of PKA activity as they migrate toward wounds<sup>36</sup>. This migration-dependent PKA gradient was resolved at super-resolution in live  $\alpha 4$ CHO cells expressing FLINC-AKAR1 (**Fig. 4a**). The difference between the normalized pcSOFI values in the leading and trailing regions was highly significant (wild type (WT), **Fig. 4b**) and was absent in cells expressing the nonphosphorylatable biosensor (TA, **Fig. 4c**). Global inhibition of PKA activity with H-89 markedly suppressed PKA activity at the leading front, whereas the trailing edge showed little change (**Supplementary Fig. 11**). The gradient observed with FLINC was approximately linear (**Fig. 4d**) and was similar to that observed with a FRET-based biosensor<sup>36</sup>. However, the super-resolution images revealed that the leading front of the cell hosted many microdomains with high PKA activity, which were absent in the trailing end. With a median diameter of approximately 280 nm, these highly active microdomains in CHO cells displayed significantly different levels of PKA activity depending on their subcellular location, and the most elevated activity was found at the filopodia. In 8/9 cells, microdomains within the filopodia, compared with the remainder of the basal membrane,

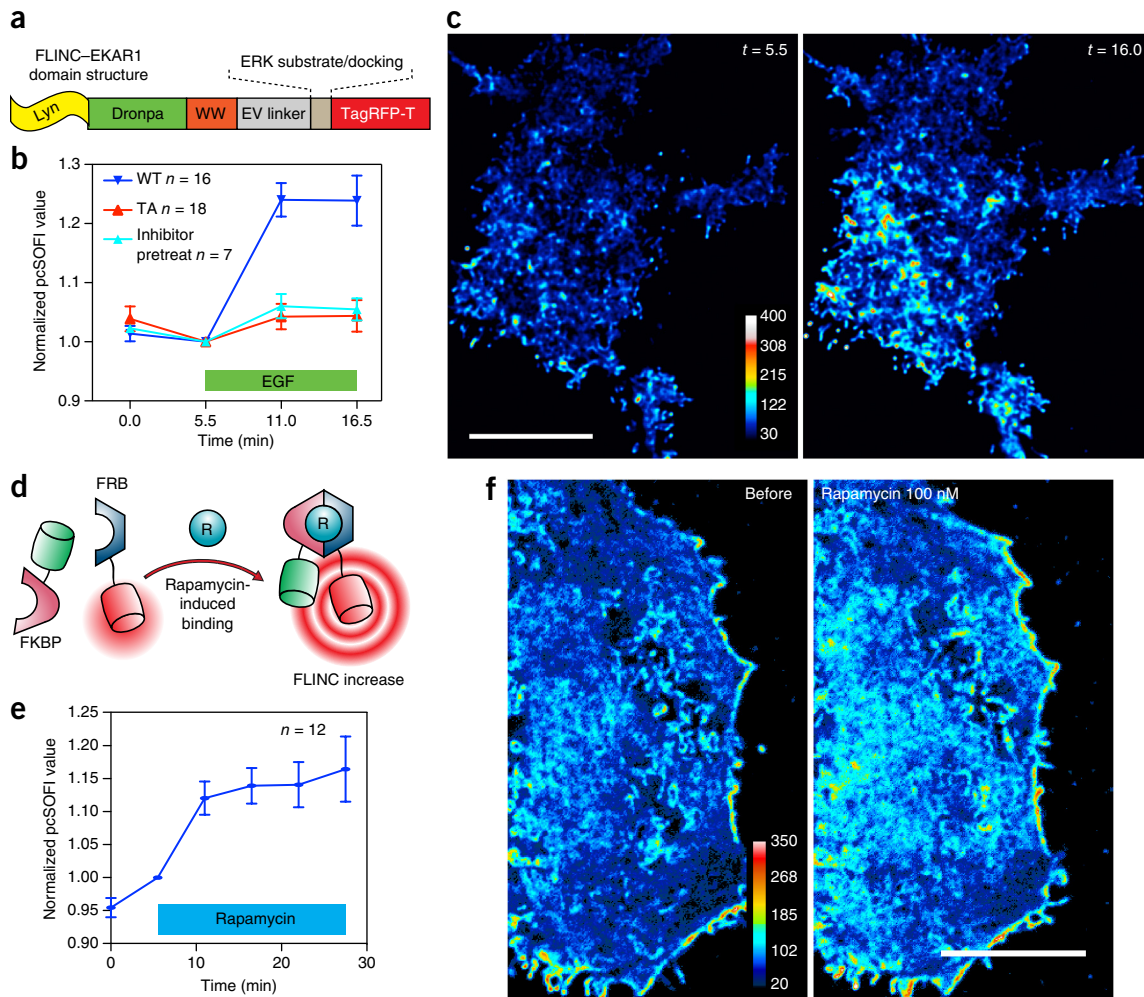


**Figure 5** | FLINC-based design is generalizable. **(a)** Domain structure of FLINC-EKAR1. **(b)** Normalized pcSOFI response time course from live HEK293 cells expressing WT FLINC-EKAR1 ( $n = 16$  cells), nonphosphorylatable mutant (TA,  $n = 18$ ) FLINC-EKAR1 and cells expressing WT but pretreated with the ERK upstream inhibitor U0126 (20  $\mu\text{M}$ ; inhibitor pretreat,  $n = 7$ ), all subjected to growth-factor stimulation (EGF 100  $\mu\text{M}$ ). **(c)** Representative super-resolution images ( $n = 16$ ) of ERK activity dynamics after growth-factor stimulation and chemical inhibition. Scale bar, 10  $\mu\text{m}$ . **(d,e)** Schematic of the design **(d)** and normalized pcSOFI time course of the bimolecular PPI sensor based on FKBP-rapamycin-FRB ( $n = 12$ ) in response to rapamycin (100 nM) **(e)**. **(f)** Normalized pcSOFI images of a HeLa cell before and after stimulation with rapamycin to induce the dimerization between FKBP and FRB. Scale bar, 10  $\mu\text{m}$ . The color scales for the before and after images are identical in **c** and **f**, respectively.

displayed a significantly higher PKA activity (**Fig. 4e**); these results are consistent with the model in which a pool of PKA molecules (such as integrin-anchored type I PKA) are highly active at the extreme tips of migrating cells<sup>37</sup>. These data suggest that distinct PKA microdomains in the same cell can have differentially regulated amplitude and spatiotemporal characteristics.

### FLINC is a general platform for biosensing

To demonstrate the generalizability of the design, we constructed a FLINC biosensor for extracellular signal-regulated kinase (ERK) activity, which was based on EKARev<sup>25</sup> (**Fig. 5a**). In HEK293 cells expressing plasma-membrane-targeted FLINC-EKAR1, pcSOFI values again provided consistent and robust ERK activity readouts. Stimulation of ERK with epidermal growth factor (EGF, 100 ng/mL) increased the averaged normalized pcSOFI value by 21–27% within 10 min (WT, **Fig. 5b**,  $n = 16$ ). Stimulation in cells expressing a nonphosphorylatable-mutant biosensor or pretreated with an upstream inhibitor

of ERK (U0126, 20  $\mu\text{M}$ ) produced no response (TA/pretreat, **Fig. 5b**). The super-resolution ERK activity maps (**Fig. 5c**) showed a similar resolution enhancement of 160 nm at second order (**Supplementary Fig. 7e**).

FLINC can also be harnessed to monitor PPI, as we demonstrated by using the inducible dimerization system of cytosolic FK506-binding protein (FKBP) and membrane-targeted FKBP12-rapamycin-binding domain<sup>38</sup> (FRB, **Fig. 5d**). Addition of rapamycin (100 nM) led to the rapid heterodimerization of FKBP and FRB, as detected by a fast increase in normalized pcSOFI value across the cell membrane, which plateaued at 15% after 20 min (**Fig. 5e,f**). When optimized, FLINC was also able to detect weaker PPI. We split FLINC-AKAR1 into two separate constructs consisting of a diffusible FHA1-Dronpa and a membrane-targeted PKA-substrate-TagRFP-T. PKA phosphorylation of the substrate recruited cytosolic FHA1 and induced a corresponding normalized pcSOFI signal increase, even though the affinity between FHA1 and phosphosubstrate is  $\sim 0.5 \mu\text{M}$

(ref. 39) (**Supplementary Fig. 12**). These examples show the generalizability of FLINC-based biosensors and their potential to enhance the dissection of spatially organized biochemical activities.

## DISCUSSION

The nanometer sensitivity of FLINC enabled us to emulate the powerful spectroscopic ruler FRET<sup>40,41</sup> and to develop new biosensors for kinase activities and PPI that are compatible with super-resolution imaging. Although the spatial resolution is not as high as that of bimolecular fluorescence complementation (BiFC)-based super-resolution methods<sup>14–16</sup>, FLINC's lack of a requirement for complementation and fluorophore maturation allowed us to achieve reversibility and a fast response in the biosensors for investigating dynamic signaling activities in live cells. FLINC-based biosensors can be created and optimized similarly to their FRET-based counterparts. Notably, a FLINC biosensor using the original compact molecular switch in AKAR2 (ref. 24) did not yield a substantial signal after PKA activation, thus demonstrating that the linker in AKAR2 is necessary to maximize the dynamic range of a FLINC biosensor. In addition to intermolecular distance, the FP orientation within a biosensor will be a crucial consideration in future designs. Although FLINC is currently limited to Dronpa and TagRFP-T, future studies will test other fluorescent protein mutants for their applicability. As in FRET-based biosensors, monomerized fluorescent proteins are preferable, although we have not observed issues arising from dimerization of TagRFP-T<sup>42</sup>.

Although we demonstrated that the relationship between pcSOFI value and FP proximity is ordinal, at this time, pcSOFI value cannot be used to directly infer molecular distance. The absolute pcSOFI values depend on biosensor expression and the optical setup (particularly camera gain and excitation intensity). However, our normalization scheme largely removes the expression dependence. Therefore, normalized pcSOFI values can be compared across experiments, as long as the imaging parameters remain identical. The current temporal resolution may fall short for tracking rapid changes. However, pcSOFI calculations can converge to a high signal-to-noise ratio<sup>43</sup> very quickly (**Supplementary Note**). Specifically, we used only 4 s of the 30-s interval to collect data. The temporal resolution will thus improve as more sensitive and faster cameras become available. In principle, as long as fluctuations can be observed, many types of illumination can be used to monitor FLINC, including epifluorescence and z-sectioning methods such as lattice light-sheet microscopy.

Under the conditions described here and previously<sup>11</sup>, diffusion does not affect the accuracy and temporal or spatial resolution of pcSOFI and its quantification of FLINC. This lack of influence is because fluorophore diffusion over the total duration of pcSOFI measurement does not lead to distortions, as long as the fluorophore motion within a single exposure (35 ms) is sufficiently small. Over the imaging time, the local environment can in fact be more thoroughly sampled by virtue of biosensor diffusion. In our experiments, we estimated that biosensor diffusion was within a single pixel during a single exposure (**Supplementary Note**); simulations using published diffusion coefficients did not reveal distortions. However, depending on the local access and sensitivity to phosphatases that reset kinase biosensors, biosensor diffusion may potentially lower the spatial resolution of the

kinase activity map. In this case, whereas the PKA activity microdomains resolved would still accurately reflect the environment experienced by any endogenous substrate, there would be a slight overestimation of the size of the PKA activation zone. However, there was no evidence that the above issue was substantial in our experiments, because the sizes of microdomains measured by the super-resolution methods STORM and FLINC were in good agreement.

To our knowledge, this study provides the first demonstration of super-resolution imaging of dynamic enzymatic activities such as protein kinase activities in living cells. PKA substrates are known to be more rapidly phosphorylated when they are localized to AKAP complexes<sup>44</sup>, in agreement with high PKA activity in the vicinity of AKAP-assembled signalosomes. Our data now reveal that the activity zone of anchored PKA is larger than the intrinsic flexibility of the PKA holoenzyme complex<sup>45</sup>. The self-clustering of AKAP79 and the coclustering of AKAP79 and p-PKAsub signals suggest that the clustering of AKAP complexes, and hence an increased effective concentration of PKA regulatory subunits, may provide an efficient means to recapture the dissociated C subunit and maintain PKA activity compartmentalization. Interestingly, 24% of total AKAP79 were orphaned and not clustered with p-PKAsub. These and other data suggest that AKAPs may maintain microdomains with varying PKA activity levels, which evolve dynamically on the basis of the associated regulatory partners such as adenylyl cyclases, phosphodiesterases, kinases and phosphatases<sup>46</sup>. Because PKA is a classical example of compartmentalized signaling, other biochemical activities may be under similarly precise spatiotemporal regulation. These spatial details and their functional roles may be illuminated with this new class of FLINC biosensors.

## METHODS

Methods, including statements of data availability and any associated accession codes and references, are available in the [online version of the paper](#).

*Note: Any Supplementary Information and Source Data files are available in the online version of the paper.*

## ACKNOWLEDGMENTS

The authors acknowledge Q. Ni, L.M. Amzel, S. Mehta and P.A. Iglesias for critical reading of the manuscript, and X. Zhou for aid in protein purification. This work was supported by NIH DP1 CA174423, R35 CA197622 and R01 DK073368 (to J.Z.); R01 GM079440, T32 GM008403 and NSF MCB 141210B (to K.G.F.); R01CA74305 (to P.A.C.); NCI1K22CA154600 and 1R03A188439 (to E.J.K.); a Research-Foundation Flanders (FWO-Vlaanderen) postdoctoral fellowship, KU Leuven Research Professorship and European Research Council ERC Starting Grant 714688 (to P.D.); and a Graduate Research Fellowship from the NSF DGE-1232825 (to A.M.P.). J.Z. and G.M. acknowledge the UCSD Specialized Cancer Center Support Grant P30 2P30CA023100-28. R.J. acknowledges NIST and the NSF Physics Frontier Center at JILA for support. R.J. is a staff member in the Quantum Physics Division of the National Institute of Standards and Technology (NIST). Certain commercial equipment, instruments or materials are identified in this paper in order to specify the experimental procedure adequately. Such identification is not intended to imply recommendation or endorsement by the NIST, nor is it intended to imply that the materials or equipment identified are necessarily the best available for the purpose.

## AUTHOR CONTRIBUTIONS

G.C.H.M. and J.Z. made the initial discovery and designed all experiments. P.D. was also involved in the initial proposal of the research direction. G.C.H.M., B.R., F.H., P.M., E.G., X.Y., C.B., B.T., A.M.P., Z.C. and K.G.F. performed experiments and analyzed data with input from J.Z., J.X., R.J., A.P., K.G.F. and P.A.C.; Y.W. and E.J.K. provided reagents. G.C.H.M., B.R., E.G. and P.D. developed

and validated all postprocessing algorithms; P.D. formalized the normalization approach. G.C.H.M. and J.Z. wrote the paper.

#### COMPETING FINANCIAL INTERESTS

The authors declare no competing financial interests.

Reprints and permissions information is available online at <http://www.nature.com/reprints/index.html>.

- Avraham, R. & Yarden, Y. Feedback regulation of EGFR signalling: decision making by early and delayed loops. *Nat. Rev. Mol. Cell Biol.* **12**, 104–117 (2011).
- Ganesan, A. & Zhang, J. How cells process information: quantification of spatiotemporal signaling dynamics. *Protein Sci.* **21**, 918–928 (2012).
- Wong, W. & Scott, J.D. AKAP signalling complexes: focal points in space and time. *Nat. Rev. Mol. Cell Biol.* **5**, 959–970 (2004).
- Rizzuto, R. & Pozzan, T. Microdomains of intracellular Ca<sup>2+</sup>: molecular determinants and functional consequences. *Physiol. Rev.* **86**, 369–408 (2006).
- Cambi, A. & Lidke, D.S. Nanoscale membrane organization: where biochemistry meets advanced microscopy. *ACS Chem. Biol.* **7**, 139–149 (2012).
- Sengupta, P., van Engelenburg, S.B. & Lippincott-Schwartz, J. Superresolution imaging of biological systems using photoactivated localization microscopy. *Chem. Rev.* **114**, 3189–3202 (2014).
- Huang, B., Bates, M. & Zhuang, X. Super-resolution fluorescence microscopy. *Annu. Rev. Biochem.* **78**, 993–1016 (2009).
- Hell, S.W. Far-field optical nanoscopy. *Science* **316**, 1153–1158 (2007).
- Betzig, E. *et al.* Imaging intracellular fluorescent proteins at nanometer resolution. *Science* **313**, 1642–1645 (2006).
- Rust, M.J., Bates, M. & Zhuang, X. Sub-diffraction-limit imaging by stochastic optical reconstruction microscopy (STORM). *Nat. Methods* **3**, 793–795 (2006).
- Dedecker, P., Mo, G.C.H., Dertinger, T. & Zhang, J. Widely accessible method for superresolution fluorescence imaging of living systems. *Proc. Natl. Acad. Sci. USA* **109**, 10909–10914 (2012).
- Dertinger, T., Colyer, R., Iyer, G., Weiss, S. & Enderlein, J. Fast, background-free, 3D super-resolution optical fluctuation imaging (SOFI). *Proc. Natl. Acad. Sci. USA* **106**, 22287–22292 (2009).
- Rego, E.H. *et al.* Nonlinear structured-illumination microscopy with a photoswitchable protein reveals cellular structures at 50-nm resolution. *Proc. Natl. Acad. Sci. USA* **109**, E135–E143 (2012).
- Liu, Z. *et al.* Super-resolution imaging and tracking of protein-protein interactions in sub-diffraction cellular space. *Nat. Commun.* **5**, 4443 (2014).
- Nickerson, A., Huang, T., Lin, L.-J. & Nan, X. Photoactivated localization microscopy with bimolecular fluorescence complementation (BiFC-PALM) for nanoscale imaging of protein-protein interactions in cells. *PLoS One* **9**, e100589 (2014).
- Hertel, F., Mo, G.C.H., Duwé, S., Dedecker, P. & Zhang, J. RefSOFI for mapping nanoscale organization of protein-protein interactions in living cells. *Cell Rep.* **14**, 390–400 (2016).
- Newman, R.H., Fosbrink, M.D. & Zhang, J. Genetically encodable fluorescent biosensors for tracking signaling dynamics in living cells. *Chem. Rev.* **111**, 3614–3666 (2011).
- Ando, R., Mizuno, H. & Miyawaki, A. Regulated fast nucleocytoplasmic shuttling observed by reversible protein highlighting. *Science* **306**, 1370–1373 (2004).
- Shaner, N.C. *et al.* Improving the photostability of bright monomeric orange and red fluorescent proteins. *Nat. Methods* **5**, 545–551 (2008).
- Arai, R., Ueda, H., Kitayama, A., Kamiya, N. & Nagamune, T. Design of the linkers which effectively separate domains of a bifunctional fusion protein. *Protein Eng.* **14**, 529–532 (2001).
- Dickson, R.M., Cubitt, A.B., Tsien, R.Y. & Moerner, W.E. On/off blinking and switching behaviour of single molecules of green fluorescent protein. *Nature* **388**, 355–358 (1997).
- Bourgeois, D. & Adam, V. Reversible photoswitching in fluorescent proteins: a mechanistic view. *IUBMB Life* **64**, 482–491 (2012).
- Geissbuehler, S. *et al.* Live-cell multiplane three-dimensional super-resolution optical fluctuation imaging. *Nat. Commun.* **5**, 5830 (2014).
- Zhang, J., Hupfeld, C.J., Taylor, S.S., Olefsky, J.M. & Tsien, R.Y. Insulin disrupts beta-adrenergic signalling to protein kinase A in adipocytes. *Nature* **437**, 569–573 (2005).
- Komatsu, N. *et al.* Development of an optimized backbone of FRET biosensors for kinases and GTPases. *Mol. Biol. Cell* **22**, 4647–4656 (2011).
- Bacskai, B.J. *et al.* Spatially resolved dynamics of cAMP and protein kinase A subunits in Aplysia sensory neurons. *Science* **260**, 222–226 (1993).
- Chen, C., Nakamura, T. & Koutalos, Y. Cyclic AMP diffusion coefficient in frog olfactory cilia. *Biophys. J.* **76**, 2861–2867 (1999).
- Neves, S.R. *et al.* Cell shape and negative links in regulatory motifs together control spatial information flow in signaling networks. *Cell* **133**, 666–680 (2008).
- Nikolaev, V.O., Bünemann, M., Hein, L., Hannawacker, A. & Lohse, M.J. Novel single chain cAMP sensors for receptor-induced signal propagation. *J. Biol. Chem.* **279**, 37215–37218 (2004).
- Saucerman, J.J., Greenwald, E.C. & Polanowska-Grabowska, R. Mechanisms of cyclic AMP compartmentation revealed by computational models. *J. Gen. Physiol.* **143**, 39–48 (2014).
- Harootunian, A.T. *et al.* Movement of the free catalytic subunit of cAMP-dependent protein kinase into and out of the nucleus can be explained by diffusion. *Mol. Biol. Cell* **4**, 993–1002 (1993).
- Wen, W. *et al.* Factors that influence the nuclear accessibility of the catalytic subunit of the cAMP-dependent protein-kinase. *FASEB J.* **8**, A1226 (1994).
- Dessauer, C.W. Adenylyl cyclase–A-kinase anchoring protein complexes: the next dimension in cAMP signaling. *Mol. Pharmacol.* **76**, 935–941 (2009).
- Dodge, K. & Scott, J.D. AKAP79 and the evolution of the AKAP model. *FEBS Lett.* **476**, 58–61 (2000).
- Wang, Y. *et al.* Isoform-selective disruption of AKAP-localized PKA using hydrocarbon stapled peptides. *ACS Chem. Biol.* **9**, 635–642 (2014).
- Lim, C.J. *et al.* Integrin-mediated protein kinase A activation at the leading edge of migrating cells. *Mol. Biol. Cell* **19**, 4930–4941 (2008).
- Lim, C.J. *et al.*  $\alpha 4$  Integrins are Type I cAMP-dependent protein kinase-anchoring proteins. *Nat. Cell Biol.* **9**, 415–421 (2007).
- Inoue, T., Heo, W.D., Grimley, J.S., Wandless, T.J. & Meyer, T. An inducible translocation strategy to rapidly activate and inhibit small GTPase signaling pathways. *Nat. Methods* **2**, 415–418 (2005).
- Durocher, D. *et al.* The molecular basis of FHA domain:phosphopeptide binding specificity and implications for phospho-dependent signaling mechanisms. *Mol. Cell* **6**, 1169–1182 (2000).
- Miyawaki, A. & Tsien, R.Y. Monitoring protein conformations and interactions by fluorescence resonance energy transfer between mutants of green fluorescent protein. *Methods Enzymol.* **327**, 472–500 (2000).
- Lakowicz, J.R. *Principles of Fluorescence Spectroscopy* 3rd edn. (Springer, 2010).
- Landgraf, D., Okumus, B., Chien, P., Baker, T.A. & Paulsson, J. Segregation of molecules at cell division reveals native protein localization. *Nat. Methods* **9**, 480–482 (2012).
- Vandenberg, W. *et al.* Model-free uncertainty estimation in stochastic optical fluctuation imaging (SOFI) leads to a doubled temporal resolution. *Biomed. Opt. Express* **7**, 467–480 (2016).
- Zhang, J., Ma, Y., Taylor, S.S. & Tsien, R.Y. Genetically encoded reporters of protein kinase A activity reveal impact of substrate tethering. *Proc. Natl. Acad. Sci. USA* **98**, 14997–15002 (2001).
- Smith, F.D. *et al.* Intrinsic disorder within an AKAP-protein kinase A complex guides local substrate phosphorylation. *eLife* **2**, e01319 (2013).
- Gold, M.G. *et al.* Architecture and dynamics of an A-kinase anchoring protein 79 (AKAP79) signaling complex. *Proc. Natl. Acad. Sci. USA* **108**, 6426–6431 (2011).

## ONLINE METHODS

**Plasmid and construct generation.** All mammalian constructs were cloned by using the pcDNA3.0 vector with a modified multiple cloning site. All *Escherichia coli* constructs were cloned by using the pRSET-B vector. Plasmids were generated through typical molecular cloning methods with a combination of PCR and restriction-enzyme cloning. PCR was always performed with Phusion polymerase (New England BioLabs) unless otherwise noted. Cloning and subcloning were performed with the *E. coli* DH5 $\alpha$  strain.

**Mutagenesis (error-prone PCR and site directed).** All site-directed mutagenesis experiments were performed according to a published protocol<sup>47</sup> with the *E. coli* JM109 strain. The randomized screen at N102 of Dronpa was performed on a WT tandem DpTT template with fully degenerate primers (NNN). Error-prone PCR was performed with Taq polymerase and an in-house dNTP mixture. Eight rounds of consecutive PCR were performed (on Dronpa only) with a reverse primer containing the 8-amino acid linker at the 3' end, thus ensuring that the linker was not subject to mutation. The mutation rate was approximated through sequencing, and the third- to fifth-round PCR products (approximately <2% point-mutation rate) were selected for further cloning. These mutant Dronpa fragments were ligated into a linearized pRSET-B plasmid containing WT TagRFP-T with BamHI and KpnI sites. All of the ligation product was transformed into JM109 cells, which were then plated onto LB-Amp agar. The candidate mutants were then screened on the basis of colony fluorescence. After a candidate was chosen, its fluorescence intensity was confirmed by averaging the fluorescence of many colonies over a larger area on the LB-Amp agar plate.

**Mutant screening.** Expression of TagRFP-T results in an intense salmon-pink color, owing to chromophore absorption. The tandem DpTT construct showed a faint but visible color. During error-prone or site-directed mutagenesis screening, we rejected any mutant that did not display this color, thereby excluding poorly folded mutants and those containing premature stop codons and frame shifts. To quantify the effects of the mutations on mutant DpTT constructs, *E. coli* (JM109) cells expressing the mutants were streaked onto LB-Amp agar plates. The mean intensity of each mutant in the GFP or RFP channel was measured with the same exposure settings on an in-house fluorescence imager, illuminated by a broad-spectrum lamp source (MAX-303, Asahi Spectra) and monitored with a Thorlabs USB digital camera mounted behind a Thorlabs emission filter wheel (maxima/bandwidth: CFP, 430/40 nm; GFP, 535/40 nm; RFP, 630/75 nm). For comparison, each plate was streaked with DpTT as well as TagRFP-T colonies as normalizing controls. The images were analyzed with ImageJ (version 1.47g). The site-directed, randomized screen at N102 of Dronpa was carried out with the same criteria outlined above. Only brightly fluorescent colonies (in both GFP/RFP channels) were sequenced.

**Cell culture, transfection and pretreatment.** The HeLa and HEK293 cells used for these experiments were between passages 20 and 65. Cells were maintained in DMEM supplemented with 10% FBS and 1% penicillin/streptomycin. CHO cells

(passage 8–22) stably expressing  $\alpha 4$  integrin were maintained in DMEM F12 with 10% FBS and 1% penicillin/streptomycin. All cells were transfected at an approximate confluency of 70% with Lipofectamine 2000 and incubated for 24 h before imaging. All cells were imaged in HBSS buffer at room temperature. To achieve AKAP-PKA RII disruption, HeLa cells were incubated with 5  $\mu$ M of the synthetic disruptor peptide STAD-2 (or its scrambled control) in DMEM for 6 h at 37 °C and 5% CO<sub>2</sub>. Immediately before imaging, the HBSS imaging buffer was supplemented with the appropriate peptide at 5  $\mu$ M. For migration studies, CHO cells were plated on cover slips coated overnight with 10  $\mu$ g/mL human fibronectin (in DPBS). For induction of migration, cells were grown to a monolayer and wounded with a 200- $\mu$ L pipette tip, then washed and incubated in HBSS buffer for 1 h before imaging.

**Epifluorescence imaging.** All epifluorescence imaging was performed on a Zeiss Axiovert 200M microscope equipped with a xenon lamp and a cooled CCD, under a 40 $\times$  oil-immersion objective. FRET microscopy of GFP/RFP biosensors such as FLINC-AKAR1 was performed with the following excitation/emission filter combinations (maxima/bandwidths): GFP, excitation 480/30 nm, emission 535/45 nm; RFP, excitation 568/55 nm, emission 653/95 nm; FRET, excitation 480/30 nm, emission 653/95 nm. All epifluorescence experiments were subsequently analyzed with MetaFluor software.

**Total internal reflection fluorescence (TIRF) imaging.** All pcSOFI TIRF imaging was performed with a Nikon Eclipse Ti microscope equipped with a Photometric Evolve 512 EMCCD, a Melles Griot argon laser (GFP excitation 488 nm) and a Coherent Sapphire solid-state laser (RFP excitation 561 nm), or was performed with a very similar Nikon N-STORM/TIRF microscope equipped with an Andor IXON3 Ultra DU897 electron-multiplying CCD camera. Cell were always imaged under a 100 $\times$  oil-immersion objective (NA 1.49) without further magnification. The TIRF condition was created with a commercial TIRF mirror setup from Nikon and was controlled electronically through the imaging software (Nikon NIS-Elements v3.22.00). All TIRF imaging was performed with electronic focus drift correction. All TIRF images or time-lapse series were captured in 16 bit without binning at 35-ms exposure. For the FLINC data set, we estimated that the 561-nm (RFP) laser intensity at the sample was 24 W/cm<sup>2</sup>. The multiplier gain and laser power were kept consistent across all FLINC experiments involving WT Dronpa (DpTT, FLINC-AKAR1, FLINC-EKAR1, FLINC-AKAR1-TA, FLINC-EKAR1-TA and FKBP-Dronpa/FRB-TagRFP-T-CAAX) reported herein. However, because mutant and control constructs displayed disparate intensities, the multiplier gain and laser power were varied to obtain proper exposure. We performed laser and multiplier-gain calibration and found both to be linear. Therefore, the data presented for mean intensity comparisons among WT DpTT, mutant DpTT and controls (**Supplementary Fig. 1b–e**) were normalized to a gain of 1 and laser power of 100% by application of the appropriate correction factor. Skewness calculations were performed with home-built Matlab software, and pcSOFI calculation and normalization were performed with Localizer software<sup>48</sup>. Post-processing algorithms are described in detail in the **Supplementary Note**.

**Statistical methods.** All statistical significance was tested with Welch's *t* test (two-sided, 95% confidence interval). All error bars indicate s.e.m. For pcSOFI and STORM measurements, single-cell responses were summarized from at least two separate experiments, each with multiple cells, over at least two passages. In the case of migrating CHO cells, cells in both WT and TA groups were excluded if their migration direction could not be unambiguously established.

**Size-exclusion chromatography (SEC).** All SEC experiments were performed on a GE ÄKTA protein purification system with a Superdex 200 column at a flow rate of 0.2 mL/min. Affinity-purified Dronpa and TagRFP-T protein stock solutions were first further purified individually with SEC. The pure fractions of each FP were then pooled, mixed at a 1:1 molar ratio and concentrated to a total protein concentration of approximately 120  $\mu\text{M}$ ; the stoichiometry was verified at 1.00:1 with absorption spectroscopy followed by spectral deconvolution. A total of 150  $\mu\text{L}$  of the mixed stock solution was subsequently examined with the same SEC parameters to resolve any additional oligomeric states present in the concentrated mixture (**Supplementary Fig. 2a**). Collected fractions were subjected to absorption spectroscopy and spectral deconvolution to determine the concentration of Dronpa and TagRFP-T in each. A peak at  $\sim 92$  kDa that was not observed in the chromatographs of the individual FPs was found to contain a stoichiometric ratio of approximately 2.5 TagRFP-T molecules to 1 Dronpa. TagRFP-T is known to form dimers at high concentrations. Because Dronpa and TagRFP-T are each 30 kDa, both size and stoichiometry verified the presence of a trimeric FP complex between a TagRFP-T dimer and a Dronpa monomer.

**Analytical ultracentrifugation (AUC).** All sedimentation velocity (SV) experiments were conducted in a Beckman-Coulter Optima XL-A analytical ultracentrifuge at 50,000 r.p.m. and 20  $^{\circ}\text{C}$ . A set of initial SV experiments were performed with purified TagRFP-T, Dronpa and their mixture at concentrations of 12, 10 and 12/10  $\mu\text{M}$ , respectively. The association constant was found to be weaker than  $10^4 \text{ M}^{-1}$ . Three further SV experiments were then collected with highly concentrated proteins: TagRFP-T alone at 171  $\mu\text{M}$ , detected at 595 nm; Dronpa alone at 172  $\mu\text{M}$ , detected at 435 nm; and a mixture of TagRFP-T (171  $\mu\text{M}$ ) and Dronpa (172  $\mu\text{M}$ ), detected at 595 nm. The individual Dronpa and TagRFP-T samples were fit to normalized  $g(s^*)$  distributions with DCDT+ (version 2.4.1) with apparent weighted-average sedimentation coefficients equal to 2.4 S and 3.7 S, respectively. The sedimentation-coefficient distribution function for the mixed sample was poorly described by a sum of noninteracting species, thus indicating an association between the two components. However, the sedimentation coefficient for the Dronpa-TagRFP-T complex could not be accurately determined because the population of the species was low. To obtain an estimate of the association constant, we further analyzed the data with SedAnal (version 6.01.6926), which allows for direct boundary fitting with mass-action equations. The above sedimentation coefficients were used in an initial fitting attempt to a simple  $A + B \leftrightarrow C$  association model, which converged poorly. We reasoned that the sedimentation coefficients might have been depressed in the mixed sample, owing to molecular crowding, and therefore set them to values 10% lower than their original estimates for subsequent fitting with a range of

sedimentation coefficients for the complex, to obtain estimates of the association constant. A typical fit is shown in **Supplementary Figure 2b**. The calculated maximum sedimentation coefficient for a spherical shape of the Dronpa-TagRFP-T complex was 5.95 S and was found with the following equation:

$$s_{max} = \frac{M(1 - \bar{v}\rho)}{N_A 6\pi\eta \sqrt{\frac{3M(\bar{v} + \delta_w \bar{v}_w)}{4N_A}}}$$

Any asymmetry in the complex shape would lead to lower sedimentation coefficients. Because the complex sedimentation coefficient could not be experimentally determined, we fit the data by fixing them at several different values to obtain the association constant (**Supplementary Table 1**), in which the  $K_a$  varied between  $1,090 \text{ M}^{-1}$  and  $6,280 \text{ M}^{-1}$  for reasonable values of the complex sedimentation coefficient. With these estimates, an  $A + B \leftrightarrow C$  model yields an estimated  $K_d$  in the range of 159  $\mu\text{M}$  to 917  $\mu\text{M}$ .

**Single-molecule fluorescence characterization.** For single-molecule imaging, 30-mm round cover glasses (no. 1, VWR) were sequentially cleaned by ultrasonication in 1% Alconox, water, ethanol and 1 M KOH. PEG and biotin-PEG (Laysan Bio) were coated on the clean cover glass according to a published protocol<sup>49</sup>. A Hybriwell (Secure-Seal, Grace) was pasted on the cover glass and sealed by epoxy. The assembled chamber was sequentially incubated with 0.01 mg/ml neutravidin, then 1 mM biotin-NTA (Biotium) in PBS for 10 min. Each step was followed by two washes in  $1\times$  PBS. Histidine-tagged purified TagRFP-T or DpTT was diluted in  $1\times$  Tris buffer with different salt (300–3,000 mM NaCl) concentrations to a final protein concentration of  $\sim 100$  pM. Immobilization was performed by incubating the final TagRFP-T or DpTT solution in the chamber for 10 min and washing once with the same buffer. Single-molecule fluorescence imaging was performed in the buffer without protein on an Olympus IX-71 inverted microscope under a  $60\times$  1.45-NA TIRFM objective. A home-built optical system with a 561-nm solid-state excitation laser (Sapphire, Coherent) and an EMCCD camera (iXon DU897E, Andor Technology) was used to examine the samples (emission, ZET488/561m, Chroma Technology). An iris aperture was used to restrict the laser spot size to  $150 \times 150$  pixels ( $\sim 700 \mu\text{m}^2$ ). The laser-power density was attenuated by an ND filter (NE10A, Thorlabs) to  $12 \text{ W/cm}^2$ . Single-molecule image streams were collected with a maximum EM gain (300) in 16-ms integration time for 2,000 frames. Molecules were detected by local-maximum searching with the ImageJ plugin ThunderSTORM<sup>50</sup>. Aggregated molecules were filtered by removal of high-intensity spots ( $>3$  sigma). The spots closer than 1 pixel (267 nm) were discarded to ensure that the signal was from single molecules. The signal of the spots in every single frame was integrated from a  $3 \times 3$  ROI centered at the ThunderSTORM detections. Background was subtracted by the whole-frame averaged intensity. The real photon count was obtained per the instructions from the camera manufacturer (Andor). The autocorrelation curves were calculated from the intensity traces of individual spots in Matlab (xcorr function) and normalized to the autocorrelation value at a time lag of zero. All autocorrelation curves were averaged to a single autocorrelation function (ACF) for each condition.

**Photophysical characterizations.** For dark-state conversion (DSC) measurements, HeLa cells expressing nuclear-localized TagRFP-T/DpTT were illuminated with a 561-nm solid-state diode-pumped laser (Genesis MX, Coherent) through a custom-built inverted microscope at an intensity of  $\sim 8\text{--}10\text{ kW/cm}^2$ . A 629/56-nm band-pass filter (Semrock) was used to remove excitation from emission. Epifluorescence from the cells was collected with a PMT (Hamamatsu Photonics), and subsequently the PMT photocurrent was converted to voltage with a custom-built transimpedance operational amplifier for better signal-to-noise ratio. Fluorescence signal was digitized with a data acquisition card (DAQ, National Instruments) at a rate of 1 MHz. Pulsed illumination was achieved with an acousto-optic modulator (AOM, Gooch & Housego, 35210-BR). Cells expressing FPs were bleached continuously for 0.1 s, and fluorescence traces were collected for further analysis. The raw fluorescence data were background-corrected and spline-fitted for smoothing. The fluorescence traces had three distinct features: a rapid decay up to a 100- $\mu\text{s}$  time scale, a flat region in the 100–1,000  $\mu\text{s}$  region and a subsequent slow decay at a microsecond timescale. Hence, the fluorescence traces were fitted with a three-exponential function with equidistant time points in log scale. The fastest time constant and its corresponding amplitude from the fitting results were considered as the DSC time constant and percentage DSC, respectively<sup>51</sup>. To measure the ground-state recovery (GSR) time constants, cells expressing nuclear-localized TagRFP-T/DpTT were excited with pulse trains with 2-ms exposure time and varying interpulse delays (dark time) ranging from 5  $\mu\text{s}$  to 10 ms. Fluorescence traces collected with pulsed excitations were used to compute the percentage recoveries with the following equation without further processing:  $\text{PR} = (\text{FR} - \text{FB})/(\text{FL} - \text{FB}) \times 100$ , where PR is the percentage recovery, and FL, FB and FR are the fluorescence intensities initially, after 2-ms exposure and after the recovery between pulses, respectively. To measure the GSR time constants, FPs were excited with pulse trains with 2-ms exposure time and varying interpulse delays (dark time) ranging from 10  $\mu\text{s}$  to 50 ms. Home-built software (Matlab) was used to compute the percentage recoveries of the fluorescence, and finally the plots of percentage recovery versus dark time were fitted with a single exponential to extract GSR time constants<sup>52</sup>. Excited-state lifetimes of purified TagRFP-T and fluorescent DpTT were measured on a Fluro Time 100 commercial TCSPC system (PicoQuant) with 560-nm laser excitation with a repetition rate of 2.5 MHz. Lifetime measurements were performed with purified proteins in PBS buffer, pH 7.4, at appropriate dilutions. **Supplementary Figure 3d** displays the fluorescence decays of the proteins and instrument response function (IRF). The fluorescence traces of the FPs were fitted with iterative deconvolution with a biexponential function, using the measured IRF of the system. The intensity-weighted-average excited-state lifetimes of TagRFP-T and DpTT were 2.45 ns and 2.40 ns, respectively. These measurements are summarized in **Supplementary Table 2**.

**Direct stochastic optical reconstruction microscopy (dSTORM) imaging.** The primary antibodies used in these experiments were mouse anti-AKAP79 (BD Biosciences, 610314) and rabbit anti-phospho-(Ser/Thr) PKA substrate (pPKAsub, Cell Signaling, 9621). The anti-AKAP79 antibody was used at a 1:50 dilution, and the anti-phospho-(Ser/Thr) PKA substrate antibody was used at a 1:200 dilution after a dilution series test was conducted. The secondary antibodies used in these experiments were AlexaFluor

568 and AlexaFluor 647 (Life Technologies) at dilutions of 1:2,000 and 1:1,000, respectively. Validation information for commercial antibodies is available on the manufacturers' websites. Saponin from quillaja bark, sodium borohydride, glutaraldehyde (GA) and normal goat serum (NGS) were from Sigma-Aldrich; paraformaldehyde (PFA) was from Electron Microscopy Sciences; glycine was from Fisher Scientific; and bovine serum albumin (BSA) was from Roche Diagnostics. Cells plated in 35-mm dishes were washed three times in HBSS and pretreated for 15 min at 37 °C (or left untreated), then washed with PBS before fixation with 4% PFA and 0.2% GA PBS for 10 min at room temperature. All subsequent steps were performed on a shaker; saponin was always used at 0.0005%; all solutions were at pH 7.4. Cells were quickly rinsed in PBS after fixation and quenched with freshly made 0.1% NaBH<sub>4</sub> ice-cold PBS. After three PBS washes of 5 min each, cells were permeabilized and blocked for 1 h at room temperature in 10% NGS + saponin PBS, then subjected to three saponin PBS washes of 5 min each. Primary antibodies were diluted to working concentrations in 1% BSA + saponin PBS. Cells were incubated with primary antibody overnight at 4 °C, then subjected to three saponin PBS washes of 5 min each. Secondary antibodies were diluted to working concentrations in 1% BSA + saponin PBS. Cells were incubated with secondary antibodies for 1 h at room temperature in the dark. All remaining steps were performed in the dark. Cells were washed three times with saponin PBS for 5 min each, then washed three times with PBS for 5 min each. All samples were postfixed in 4% PFA PBS for 10 min at room temperature and quickly rinsed in PBS and quenched with three washes in 100 mM glycine PBS for 5 min each. The cells were washed three times in PBS for 5 min each and stored in PBS at 4 °C in the dark until imaging within 24 h. All STORM imaging was performed on a Nikon Ti microscope under total internal reflection conditions, with a 100 $\times$  1.49-NA Apo TIRF objective. Images were collected within a 256  $\times$  256 pixel ROI on an Andor IXON3 Ultra DU897 electron-multiplying CCD camera with the multi-color continuous mode setting in Nikon Elements software. The power of the 568-nm and 647-nm excitation (as well as activating 405-nm excitation) was adjusted to enable stochastic blinking behavior within the ROI. The images were reconstructed and drift-corrected with Nikon N-STORM software. Postprocessing of the STORM data is described in **Supplementary Note**.

**Software availability.** Localizer software is freely available at <https://bitbucket.org/pdedecker/localizer/>. The Matlab software is available upon reasonable request.

**Data availability.** Addgene codes are available for the following constructs: DpTT, [87704](#); FLINC-AKAR1, [87705](#); FLINC-AKAR-TA, [87706](#); FLINC-EKAR1, [87707](#); FLINC-EKAR-TA, [87708](#); FKBP-Dp, [87709](#); FRB-TT-CAAX, [87710](#); Dp-FHA1, [87711](#); PKAsub-TT-CAAX, [87712](#); and PKAsub(TA)-TT-CAAX, [87740](#). The data supporting the present findings are available upon reasonable request.

47. Sawano, A. & Miyawaki, A. Directed evolution of green fluorescent protein by a new versatile PCR strategy for site-directed and semi-random mutagenesis. *Nucleic Acids Res.* **28**, E78 (2000).

48. Dedecker, P., Duwe, S., Neely, R.K. & Zhang, J. Localizer: fast, accurate, open-source, and modular software package for superresolution microscopy. *J. Biomed. Opt.* **17**, 5 (2012).

49. Roy, R., Hohng, S. & Ha, T. A practical guide to single-molecule FRET. *Nat. Methods* **5**, 507–516 (2008).
50. Ovesný, M., Křížek, P., Borkovec, J., Svindrych, Z. & Hagen, G.M. ThunderSTORM: a comprehensive ImageJ plug-in for PALM and STORM data analysis and super-resolution imaging. *Bioinformatics* **30**, 2389–2390 (2014).
51. Dean, K.M. *et al.* Analysis of red-fluorescent proteins provides insight into dark-state conversion and photodegradation. *Biophys. J.* **101**, 961–969 (2011).
52. Manna, P. & Jimenez, R. Time and frequency-domain measurement of ground-state recovery times in red fluorescent proteins. *J. Phys. Chem. B* **119**, 4944–4954 (2015).